# Temperature dependence of the velocity-density relation for liquid metals under high pressure: implications for the Earth's outer core

-REVISION 1-

Tetsuya Komabayashi[1,2,*], Jinya Kato[1], Kei Hirose[3,4], Satoshi Tsutsui[5], Saori Imada[1], Yoichi Nakajima[6] and Alfred Q. R. Baron[5,6].

[1] Department of Earth and Planetary Sciences, Tokyo Institute of Technology, 2-12-1 Ookayama, Meguro, Tokyo 152-8551, Japan

[2] Now at School of GeoSciences and Centre for Science at Extreme Conditions, University of Edinburgh, Grant Institute, The King's Buildings, James Hutton Road, Edinburgh EH9 3FE, UK

[3] Earth-Life Science Institute, Tokyo Institute of Technology, 2-12-1 Ookayama, Meguro, Tokyo 152-8551, Japan

[4] Laboratory of Ocean-Earth Life Evolution Research, Japan Agency for Marine-Earth Science and Technology, 2-15 Natsushima-cho, Yokosuka, Kanagawa 237-0061, Japan

[5] SPring-8, Japan Synchrotron Radiation Research Institute, 1-1-1 Kouto, Sayo-cho, Sayo-gun, Hyogo 679-5198, Japan

[6] Material Dynamics Laboratory, RIKEN SPring-8 Center, RIKEN, 1-1-1 Kouto, Sayo-cho, Sayo-gun, Hyogo 679-5198, Japan

*corresponding author: Tetsuya Komabayashi
School of GeoSciences and Centre for Science at Extreme Conditions,
University of Edinburgh
Edinburgh EH9 3FE, UK
Tel: +44-(0)131-650-8518 Fax: +44-(0)131-650-7340
E-mail: tetsuya.komabayashi@ed.ac.uk

## ABSTRACT

The relationship between the sound velocity, density, and temperature of liquid metals is important when one tries to interpret the seismic velocity profile and infer the chemical compositions of the Earth's outer core. We therefore, have experimentally measured the longitudinal acoustic (LA) velocity of liquid indium under high *P-T* conditions. Also, we examine a Hugoniot data of liquid iron by comparing with an existing equation of state (EoS). The LA velocities of liquid and solid indium at pressures up to 6.7 GPa and temperatures mostly at 710 K were measured using inelastic X-ray scattering (IXS) to probe samples in an externally-heated diamond anvil cell. A thermal EoS for liquid indium derived from existing literature was used to calculate the density for the IXS measurements and to provide an independent check on the sound velocities. The IXS data are consistent with the hydrodynamic LA velocity derived from the liquid EoS, implying that the positive dispersion is minimal in liquid indium. The velocity-density relation for liquid indium derived from the EoS has temperature dependence, implying that Birch's law does not hold for the liquid phase. Similarly we calculated the temperature-velocity-density relation of liquid iron over the Earth's core range from a recently reported EoS. The resulting velocity-density relation is also temperature dependent, indicating that liquid iron thus

54 does not follow Birch's law. The violation of Birch's law implies that the Hugoniot
55 data cannot be directly compared with seismological observations because of the
56 different temperature ranges. Formulation of the temperature-velocity-density of liquid
57 iron-alloys supported by experimental measurements provides better understanding of
58 the thermodynamic state of the Earth's core.
59

60 **INTRODUCTION**

61 The relationship between the sound velocity and the density and/or pressure
62 ($P$) of an Earth-forming material is important when one tries to interpret the seismic
63 velocity profile and infer the chemical compositions of the deep Earth. Birch (1961)
64 empirically found that the longitudinal acoustic (LA) sound velocity of rock-forming
65 materials with the same mean atomic weight scales linearly with density, namely
66 Birch's law. In other words, compression of a material would give a straight line in a
67 plot of velocity against density. The utility of Birch's law is that the effect of
68 temperature ($T$) on the sound velocity of the material appears only through the density
69 (i.e., thermal expansion) and therefore, one is not required to examine the temperature
70 effect on the sound velocity of a material, or to consider the temperature in the deep
71 Earth, which is one of the least constrained properties. The applicability of Birch's law

has been relatively well investigated for solids, particularly iron-alloys, with implications for the inner core (Fiquet et al., 2001; Badro et al., 2007; Antonangeli et al., 2010; Shibazaki et al., 2012). The background physics for Birch's law which holds for crystalline solids up to moderate temperatures, but not close to the melting point, lies in the atomic dynamics which is described within a quasiharmonic approximation (Chung, 1972; Antonangeli et al., 2012).

For liquid metals, the velocity-density relation has not been investigated as much as for solids. Most reported data were obtained at 1 bar, or from shock wave experiments. Recently Sakaiya et al. (2014) conducted a laser-pulse experiment on liquid iron and demonstrated that the density-velocity data along a Hugoniot can be expressed as a straight line, and they suggested that Birch's law might hold for liquid iron. They also suggested that Birch's law may apply to various metal liquids, from existing Hugoniot data on other metals showing similar changes in the properties between solid and liquid. However, the pressure and temperature simultaneously rise along the Hugoniot in the shock wave experiments, which makes it difficult to separate the effects of the two parameters. As such, there remains the possibility that while the Hugoniot velocity-density path in Sakaiya et al. (2014) can be described as the straight line, different Hugoniot paths (e.g., with a pre-heated starting material) may go through

different trajectories, and the material may not obey Birch's law.

Static experiments make it possible to collect data over a wide *P*-*T* range and investigate pressure and temperature dependences separately. They are however, even rarer since melting usually requires a high temperature. In addition to the difficulty of attaining simultaneous high-*P*-*T* conditions, measuring the sound velocity of materials at static high pressures is challenging. In the present study, we measured the LA velocity of liquid indium under high pressures (to 6.7 GPa) mostly at 710 K, using inelastic X-ray scattering (IXS) from a sample held in an externally resistively-heated diamond anvil cell (DAC). Among metals, indium has been relatively well studied due to its low melting temperature (Hill and Ruoff, 1965; Kamioka, 1983; Shen et al., 2002ab; Alatas et al., 2008). Hill and Ruoff (1965) investigated the LA velocity of liquid indium at atmospheric pressure from 440 to 618 K, using ultrasonic pulse experiments, while IXS has previously been used to investigate sound velocities in ambient conditions (Reichert et al., 2007) and under modest high-pressure conditions ($P$ = 1.7-4.0 GPa and $T$ = 513-633 K) (Alatas et al., 2008). We expanded the *P*-*T* range to investigate the temperature-pressure (density)-LA velocity relations, namely if Birch's law is violated or not.

IXS has become an accepted technique to measure the sound velocity of

polycrystalline solids in a DAC. However interpretation of IXS measurements of liquids can be complicated because many liquids, including metals, show an effect called positive dispersion. This causes the LA velocities estimated from IXS at shorter correlation lengths to exceed the hydrodynamic (long wavelength) sound velocity (e.g., Scopigno et al., 2005). Another way to derive the velocity-density relation for a liquid is use of a thermal equation of state (EoS) which describes density (molar volume)-pressure-temperature relation (e.g., Komabayashi, 2014). Such an EoS provides the information necessary to calculate the LA velocity for liquids, in the long wavelength limit, assuming the shear modulus is zero. We investigate the presence of the positive dispersion by the comparison of the IXS velocity and the hydrodynamic LA velocity derived from the EoS.

In the present work we experimentally measured the LA velocity of liquid indium under high *P-T* conditions to better understand the temperature-pressure (density)-velocity relation in liquid metals. We also took IXS data of the solid phase for comparison. A thermal EoS for liquid indium was evaluated from existing literature data to calculate the density and the hydrodynamic LA velocity of the liquid phase. On the basis of these results, we discuss the presence of a positive dispersion and temperature dependence of the velocity-density relation in liquid indium. Finally, we

126 examine a Hugoniot data of liquid iron by comparing with an existing EoS and discuss
127 if Birch's law holds for liquid iron under terrestrial planetary core conditions.
128

129 **EXPERIMENTAL PROCEDURE**

130 High-pressure and -temperature experiments were conducted in an
131 externally-heated DAC (Noguchi et al., 2013). A pair of diamond anvils with 450-μm
132 culet and a rhenium gasket were used for high pressure generation. Heating was
133 achieved by running a DC current through a platinum heating wire made just outside
134 the diamonds. The temperature was measured using a Pt-13%Rh (R-type) or
135 Alumel-Chromel (K-type) thermocouple placed about 0.5 mm from the sample. The
136 temperature uncertainty was less than 15 K at 710 K (Noguchi et al., 2013). Powdered
137 indium (99.999% purity) was loaded into the 200-μm hole of the rhenium gasket and
138 compressed between the diamond anvils. At room temperature, the pressure was
139 determined off-line by the ruby fluorescence technique (Mao and Bell, 1986). At high
140 temperature, however, it is necessary to consider the effect of thermal expansion of the
141 pressure cell. This was done in two steps, with, first the melting point determined from
142 where the crystal X-ray diffraction (XRD) spots, as seen in an area detector,
143 disappeared and instead, diffuse signals appeared. The known melting curve (Shen et

al., 2002a) then allows determination of the pressure at the melting point with the uncertainty of 0.2-0.25 GPa (could be larger at $P > 6$ GPa as discussed later) depending on the slope of the melting curve and the temperature uncertainty in the DAC. We then extrapolated the *P*-*T* trajectory within the liquid stability field to the temperatures where the IXS measurements were made (see Fig.1).

IXS experiments were conducted at BL35XU (Baron et al., 2000) of SPring-8 in Japan. A backscattering geometry with the silicon (999) Bragg reflection was used to provide an over-all energy resolution of about 3.0 meV at 17.794 keV. The systematic error in energy scale is estimated to ~0.5% or better (Fukui et al., 2008). The beam was focused to 80-μm by 80-μm in the full width at half maximum (FWHM). Scattered photons were collected by twelve spherical silicon crystal analyzers. The momentum transfer $Q$ was set in the range of 3.0-6.4 $nm^{-1}$ (2.1-5.5 $nm^{-1}$ in the sixth run) with a resolution of 0.45 $nm^{-1}$ at FWHM. During measurements, the DAC was held in a He-filled bag or vacuum chamber in order to reduce background from air-scattering.

## RESULTS

Six sets of high-*P*-*T* IXS measurements were conducted. Experimental *P*-*T* conditions are shown in Fig. 1 and results are listed in Table 1. Typical XRD images

and IXS spectra are presented in Figs. 2 and 3 respectively.

In the first run, the IXS spectra of solid indium were collected at 1 GPa and 300 K. The sample was subsequently heated with the external heating system and the melting of indium was observed, namely the solid XRD spots disappeared and diffuse signals appears, at 514 K corresponding to 1.8 GPa based on the existing melting curve (Shen et al., 2002a). We collected the IXS spectra of liquid indium at 1.8 GPa and 517 K. After quenching to room temperature, the sample was reheated and the melting took place at 519 K and 1.8 GPa. The pressure at 300 K before the second heating cycle was not measured and therefore assumed to be 1.0 ± 0.5 GPa. The uncertainty was reduced with heating to the melting temperature at which the pressure was precisely known but again increased with further heating. We collected the IXS spectra of liquid indium at 2.2 ± 0.2 GPa and 612 K. We further increased the temperature and collected the IXS spectra of the liquid sample at 2.6 ± 0.5 GPa and 710 K. Typical data collection times were about 5 to 6 hours for a measurement of one set of 12 spectra at one *P*-*T* condition.

In the second to sixth runs, we only made a single heating cycle in each run except for the third run which collected the IXS data only at 5 GPa and 300 K. Similar to the first run, we determined the experimental *P*-*T* trajectory from the pressures at

300 K and at the melting points in order to estimate the pressures at the IXS measurements of the liquid state. In the fourth and fifth runs, we heated the sample without collecting the data at 300 K and took the IXS spectra of the liquid at high temperatures. In the sixth run the pressure before heating was 3.3 GPa but we observed melting at 531 K corresponding to 2.3 GPa, which indicates the pressure was dropped during heating. This makes it difficult to estimate the precise pressure upon further heating in the liquid stability field because, in an external heating system, the pressure would remarkably be reduced once it starts dropping. Hence the nominal pressures for the sixth run listed in Table 1 and illustrated in Fig. 1 should be taken as the maximum values.

Fig. 3 shows the IXS spectra of the fifth run at 6.5 GPa and 710 K. Analysis of the data of the liquid phase was made with the damped harmonic oscillator (DHO) model (Fåk and Dorner, 1997) convolved with the measured resolution function. The peak at the zero-energy transfer corresponds to the quasi-elastic contribution whereas the two smaller side peaks are the Stokes and anti-Stokes LA phonon signals of liquid indium. These inelastic contributions shift toward higher energy transfer with increasing $Q$ value, so that the inelastic contribution from diamond moves out of the energy transfer window for $Q > 4$ nm$^{-1}$. Fig. 4 shows the phonon excitation energy ($E$)

as a function of $Q$ (i.e., dispersion) for liquid indium at 710 K and different pressures. In all cases, the phonon excitation energy was coincident with the peak of the current-current correlation function calculated from the DHO model; a comparison is shown in Fig. 5. Data analysis of the solid phase was made with a Pseudo-Voigt function that reflects the resolution function.

The long-wavelength, $Q \rightarrow 0$ limit, LA velocity was derived from the fitting of the $Q$-$E$ dispersion data. We analyzed the IXS data of liquid indium with two fitting procedures. An example with the data at 2.6 GPa and 710 K (1st run) is described here and shown in Fig. 5. First, we fit only the $Q \sim 3$ nm$^{-1}$ with a line through the origin. The fitting yielded the LA velocity to be 2594 ± 44 m/s and the resulting dispersion line is shown in Fig. 5. In order to understand the dispersion relations over the entire $Q$ ranges in the present IXS, the second fitting was based on a sine function in analogy to crystalline solids. We take

$$\omega(Q) = c_0 Q_{ZB} \sin\left[\frac{\pi}{2}\frac{Q}{Q_{\mathrm{ZB}}}\right](1 + f(Q))$$

where $c_0$ is the long-wavelength sound speed, $Q_{\mathrm{ZB}}$ is the position of the pseudo-zone boundary (in this case a free fit parameter) and $f(Q)$ gives the magnitude of the positive dispersion. $f(Q)$ is then taken to have zero magnitude and derivative in the limit of $Q \rightarrow 0$, returning $c_0$ as the required hydrodynamic limit. For the purposes of analysis of

the present data set, we assume that, over the range of momentum transfers and thermodynamic conditions measured here, the form of $f(Q)$ is independent of the thermodynamic conditions, allowing us to make relative comparisons of the sound speed. Then our best estimate of the velocity, for the purposes of a relative comparison is given by

$$E\,[\mathrm{meV}] = 4.192 \times 10^{-4}\, V_P\,[\mathrm{m/s}] \times Q_{ZB}\,[\mathrm{nm^{-1}}] \sin\left[\frac{\pi}{2}\frac{Q\,[\mathrm{nm^{-1}}]}{Q_{ZB}\,[\mathrm{nm^{-1}}]}\right] \quad (1)$$

where $V_P$ is an experimental $Q \rightarrow 0$ limit of the IXS data, for LA velocity but does not necessarily coincide with $c_0$ for the liquid phase due to the possible presence of positive dispersion.

Twelve spectra recorded at eight distinct momentum transfers have been used for the fitting to constrain $V_P$ and $Q_{ZB}$ for each set of thermodynamic conditions in most of the runs. The fitting of the IXS data at 2.6 GPa and 710 K yielded $V_P$ = 2637 ± 42 m/s which is slightly faster but fairly consistent with the result of the linear function fitting, suggesting our approximation of $f(Q)$~constant is reasonable for $Q$ > 3nm$^{-1}$. The fitted dispersion curve is also shown in Fig. 5. Thus, we made these two fitting procedures on the IXS data at the other $P$-$T$ conditions. For the sixth run, we collected IXS data at $Q$ = 2.1-5.5 nm$^{-1}$. However, the data at Q ~2 nm$^{-1}$ were not well fitted and the phonon peaks were not resolved due to overlapping with the quasi-elastic peak.

Hence we used nine spectra at $Q$ = 3.2-5.5 nm$^{-1}$ for the fitting. Note that in the following discussions, the IXS velocity for liquid indium is from the linear fitting.

For the solid phase, in contrast to the liquid phase, $V_P$ in the equation (1) corresponds to $c_0$, and therefore the sine fit was employed to the $Q$-$E$ dispersion data. The LA wave velocities are summarized in Table 1.

Fig. 6 summarizes the LA velocity for both liquid and solid indium from IXS against the pressure together with the previous IXS data (Alatas et al., 2008). Our measurements are fairly consistent with the data of Alatas et al. (2008) confirming the precision of both experimental works.

## DISCUSSION

### Thermal equation of state for liquid indium

In order to discuss the velocity-density relation of liquid indium and to calculate $c_0$, within the thermodynamic framework, we derived a thermal EoS for liquid indium based on existing literature. A Vinet EoS was employed,

$$P_{430} = 3K_{0,430}\mathrm{x}^{-2}(1-\mathrm{x})\exp\left[\frac{3}{2}(K'-1)(1-\mathrm{x})\right] \quad (2)$$

where $\mathrm{x} \equiv (V_{P,430}/V_{0,430})^{1/3}$ and $P_{430}$, $V_{P,430}$, $K_{0,430}$, $K'$, and $V_{0,430}$ are the pressure at 430 K that is the melting temperature at 1 bar, the molar volume at $P_{430}$, the isothermal bulk

modulus, its pressure derivative, and the molar volume at 1 bar and 430 K, respectively.

The molar volume at *P*-*T* of interest, $V_{P,T}$ is expressed as,

$$V_{P,T} = V_{P,430} \exp \int_{430}^{T} \alpha_P \, dT \quad (3)$$

where $\alpha_P$ is the thermal expansion coefficient at *P* of interest. We express $\alpha_P$ as a function of pressure in the framework of the Anderson-Grüneisen expression (Anderson et al., 1992), described as,

$$\left(\frac{\alpha_P}{\alpha_0}\right) = \left(\frac{V_{P,430}}{V_{0,430}}\right)^{\delta_T} \quad (4)$$

where $\alpha_0$ is the thermal expansion coefficient at 1 bar. The parameter $\delta_T$ is so-called Anderson-Grüneisen parameter. $\delta_T$ may depend on the volume but is assumed to be constant in this study because the compression range studied here is small (to 13%) (Chopelas, 1990; Boehler et al., 1990).

Kamioka (1983) evaluated $V_{0,430}$, $K_{0,430}$, and $\alpha_0$ to be 16.33 $cm^3$ $mol^{-1}$, 32.8 GPa, and $12*10^{-5}$ $K^{-1}$, respectively. He also derived the temperature dependence of the bulk modulus (i.e., *dK*/*dT*) at 1 bar to be -0.018 GPa $K^{-1}$. We evaluated $\delta_T$ to be 5.5 ± 0.2 to yield this *dK*/*dT* value. The remaining parameter, *K'* for the liquid phase was evaluated to be 5.5 ± 0.1 so that the molar volume and bulk modulus for liquid indium at 300 K (i.e., hypothetical liquid) are larger and smaller respectively, than the solid phase (Takemura, 1991) in the pressure range studied here. The compression curves for

liquid indium calculated from those parameters are drawn in Fig. 7 together with experimental data for liquid and solid for comparison (Takemura, 1991; Shen et al., 2002b). From an X-ray absorption method, Shen et al. (2002b) estimated the density of liquid indium under high *P*-*T* conditions and reported its compression behavior at 710 K up to 8.5 GPa. Shen et al. (2002b)'s liquid data at 710 K however gives smaller volumes than solid indium at 300 K at high pressures (Fig. 7), indicating that their data did not well constrain the liquid volume. Using the newly constrained thermoelastic parameters, we calculated the density of liquid indium at the IXS measurements. Results are listed in Table 1.

From the EoS, we calculated $c_0$ of liquid indium from

$$c_0 = \sqrt{\frac{K_S}{\rho}} \quad (5)$$

where $K_S$ and $\rho$ are the adiabatic bulk modulus and density, respectively. Since the EoS yields the isothermal bulk modulus ($K_T$), conversion of it to $K_S$ is necessary which is expressed as,

$$K_S = K_T(1+\underline{\alpha_P}\gamma T) \quad (6)$$

where $\gamma$ is the Grüneisen parameter. For liquid indium, $\gamma$ is 2.5 at 430 K and 1 bar (Kamioka, 1983). As well as $\delta_T$, we assumed the constant $\gamma$ at any given *P*-*T* condition because of the low compression range studied here.

287

288 **Temperature dependence of the velocity-density relation in liquid indium**

289 Fig. 8 shows density-velocity relations for liquid indium with previously
290 published data of various measurements for comparison (Ultasonic: Hill and Ruoff,
291 1965; Kamioka, 1983; IXS: Alatas et al., 2008; this study). The liquid densities were
292 derived from the EoS constructed in this study. From the EoS parameters constructed
293 above, we also calculated $c_0$ for liquid indium at 500, 700, and 900 K (Fig. 8). The
294 calculated isothermal lines clearly indicate that the velocity-density relation is
295 temperature dependent, meaning that Birch's law does not hold; if Birch's law is
296 applicable, every isothermal line must be the same straight line.

297 The velocity obtained from the EoS is, in more detail, compared with that
298 from the IXS measurements in Fig. 9. The velocities from the IXS are fairly consistent
299 with the calculated results, i.e., $c_0$. Note that the data of the sixth run can be more
300 consistent with $c_0$ since they could overestimate the pressure (and therefore density) as
301 stated above; if the pressure is lowered, the density will be accordingly lowered, and
302 the resulting velocity will be faster. The IXS data at 6.5 and 6.7 GPa show slightly
303 faster velocities than the calculations by 2.3-2.9% (considering the uncertainties).
304 Possible explanations for those deviations include (1) another source of uncertainty

305 which is in the existing melting curve (Shen et al., 2002a) and (2) positive dispersion
306 (Scopigno et al., 2005). (1) The melting curve of indium was not tightly constrained
307 above 6 GPa so that there might be an additional uncertainty in the determination of
308 the melting pressure in this study (Fig. 1). The pressure of the 6.7 GPa and 710 K data
309 could be 7.2 GPa when the additional uncertainty is considered, which reduces the
310 above deviation to 1.1%. (2) Liquid phases could behave like solids near the melting
311 points and such solid-like liquids often show the positive dispersion (Scopigno et al.,
312 2000). Nevertheless, the small deviation of the IXS velocity from $c_0$ implies the effect
313 of the positive dispersion is minimal. The overall agreement in Fig. 9 suggests that the
314 IXS data yield $c_0$ and that the temperature dependence shown by the EoS calculations
315 is validated by the IXS measurements.
316
317 **Velocity-density relation in liquid iron and the Earth's outer core**
318 We have demonstrated that the temperature dependent velocity-density
319 relation for liquid indium derived from the EoS is supported by our IXS measurements.
320 In this section, we will derive the velocity-density relation for liquid iron from an
321 existing EoS and compare it with shock wave experimental data.
322 Komabayashi (2014) established a thermal EoS for liquid iron by constructing

323 a self-consistent thermodynamic database in the system Fe-FeO which reproduces the
324 latest static experimental data on solid phase relations, end-member melting
325 temperatures, binary melting relations, and EoS for solid phases. From the Gibbs free
326 energy calculations, he also obtained $\gamma$ which is needed for converting $K_T$ to $K_S$
327 (equation 6). As employed on liquid indium, we made velocity-density plots for liquid
328 iron at 136-350 GPa and 5000-7000 K from the database of Komabayashi (2014) (Fig.
329 10). Note that we ignored the stability of liquid in the calculations, namely the
330 properties were calculated partly in the solid iron stability as well. Existing shock wave
331 data for liquid iron are also plotted in Fig. 10 (Brown and McQueen, 1986; Sakaiya et
332 al., 2014). Same as for liquid indium, the calculated velocity-density relation for liquid
333 iron is temperature dependent, indicating that Birch's law does not hold. Moreover the
334 slopes of the isothermal line are different from that of the shock wave Hugoniot path.
335 Each Hugoniot data point however is consistent with the calculated velocity-density
336 lines at least up to 7228 K (Brown and McQueen, 1986) (Fig. 10). These comparisons
337 imply that the calculated isothermal lines are consistent with the shock wave data and
338 they clearly show that Birch's law does not hold for liquid iron. This suggests that
339 Sakaiya et al. (2014) would have misinterpreted the Hugoniot data and concluded that
340 the velocity-density relation for liquid iron would follow Birch's law. Along each

isothermal compression and each Hugoniot path, the velocity-density plot can be expressed as a straight line, but this does not necessarily mean that the material follows Birch's law.

Fig. 11 shows pressure-velocity relations of liquid iron over the outer core pressure at different temperatures, which were calculated from the data in Komabayashi (2014). The $P$-$c_0$ relation does not show temperature dependence, which confirms the violation of Birch's law since the density changes as the temperature is changed. The same results were obtained from a shock wave EoS (Anderson and Ahrens, 1994) and first-principles calculations (Vočadlo et al., 2003). Note that the negligible temperature dependence in the $P$-$c_0$ relation in pure iron would not be relevant to all the metals. Indeed liquid indium shows temperature dependence in the $P$-$c_0$ relation (Fig. 6).

Violation of Birch's law in liquid iron implies that the Hugoniot line cannot be directly compared with seismological data because the temperatures in the Hugoniot (6000-23000 K) were different from those in the core (~5000-6000 K). Contrary, the isothermal compression lines at 5000-7000 K can be compared with the seismological data such as the Preliminary Reference Earth Model (PREM) (Dziewonski and Anderson, 1981). Fig. 10 shows the Hugoniot data and calculated isothermal

359 compression lines for pure iron together with the outer core properties of the PREM.
360 The pure iron data are placed at the high density and low velocity side of the outer core
361 line, and this mismatch can be accounted for by the presence of light elements in the
362 core. However the Hugoniot line is steeper than the PREM while the isothermal lines
363 are gentler. Hence the choice of pure iron line significantly affects the resulting nature
364 of the light elements in the core.
365

366 **IMPLICATIONS**

367 The above discussions clearly indicate that Birch's law is not applicable for
368 liquid indium and iron. Many crystalline solids follow Birch's law because the atomic
369 dynamics can be described within the quasiharmonic approximation (Chung, 1972;
370 Antonangeli et al., 2012). For liquids it would not be reasonable to assume the same
371 approximation, although detailed investigations of the atomic dynamics should be
372 made in the future. As such, temperature dependent velocity-density relation should be
373 a universal nature for the liquid metals.

374 Assuming that light element-bearing iron alloys do not follow Birch's law
375 either, the temperature effect on the velocity-density relation for those alloys should be
376 clarified. A potential approach is to evaluate a thermal EoS (+ $\gamma$) and test it with

experimental measurements such as the IXS, as was employed in this study. Recently, Umemoto et al. (2014) conducted first-principles calculations on the sound velocity of iron-sulfur alloys and tested it by comparing with high-*P*-*T* IXS measurements. For extremely high-*P*-*T* conditions such as corresponding to the cores of super-Earths, EoS can be tested with shock wave experimental data (e.g., Brown and McQueen, 1986; Sakaiya et al., 2014). Formulation of the temperature-velocity-density of liquid iron-alloys supported by experimental measurements as was shown in this study provides better understanding of the thermodynamic state of the Earth's core.

## Acknowledgments

An anonymous reviewer is acknowledged for his/her constructive comments which greatly improved the manuscript. The synchrotron IXS experiments were performed at BL35XU, SPring-8 (Proposal No. 2011A1300 and 2011B1336). This research was supported in part by the JSPS Grant-in-Aid for Scientific Research and in part by the University of Edinburgh.

## References

Alatas, A., Sinn, H., Zhao, J.Y., Said, A.H., Leu, B.M., Sturhahn, W., Alp, E.E., Shen, G.Y., and Prakapenka, V.B. (2008) Experimental aspects of inelastic X-ray scattering studies on liquids under extreme conditions (P-T). High Pressure Research, 28, 175-183.

Anderson, W.W., and Ahrens, T.J. (1994) An equation of state for liquid iron and implications for the Earth's core. Journal of Geophysical Research, 99, 4273-4284.

Anderson, O.L., Oda, H., and Isaak, D.G. (1992) A model for the computation of thermal expansivity at high compression and high temperatures: MgO as an example. Geophysical Research Letters, 19(19), 1987–1990, doi:10.1029/92GL02145.

Antonangeli, D., Komabayashi, T., Occelli, F., Borissenko, E., Walters, A.C., Fiquet, G., and Fei, Y.W. (2012) Simultaneous sound velocity and density measurements of hcp iron up to 93 GPa and 1100 K: An experimental test of the Birch's law at high temperature. Earth and Planetary Science Letters, 331, 210-214.

Antonangeli, D., Siebert, J., Badro, J., Farber, D.L., Fiquet, G., Morard, G., and Ryerson, F.J. (2010) Composition of the Earth's inner core from high-pressure sound velocity measurements in Fe-Ni-Si alloys. Earth and Planetary Science Letters, 295, 292-296.

Badro, J., Fiquet, G., Guyot, F., Gregoryanz, E., Occelli, F., Antonangeli, D., and Matteo, d.A. (2007) Effect of light elements on the sound velocities in solid iron: implications for the composition of Earth's core. Earth and Planetary Science Letters, 254, 233-238.

Baron, A.Q.R., Tanaka, Y., Goto, S., Takeshita, K., Matsushita, T., and Ishikawa, T. (2000) An X-ray scattering beamline for studying dynamics. Journal of Physics and Chemistry of Solids, 61, 461-465.

Birch, F. (1961) The velocity of compressional waves in rocks to 10 kilobars, part 2. Journal of Geophysical Research, 66, 2199-2224.

Boehler, R., von Bargen, N., and Chopelas, A. (1990) Melting, thermal expansion, and phase transitions of iron at high pressures. Journal of Geophysical Research, 95, 21731-21736.

Brown, M.J., and McQueen, R.G. (1986) Phase transitions, Grueneisen parameter, and

elasticity for shocked iron between 77 GPa and 400 GPa. Journal of Geophysical Research, 91, 7485-7494.

Chopelas, A. (1990) Thermal expansion, heat capacity, and entropy of MgO at mantle pressures. Physics and Chemistry of Minerals, 17, 142-148.

Chung, D.H. (1972) Birch's Law - Why is it so good. Science, 177, 261-263.

Dziewonski, A.M., and Anderson, D.L. (1981) Preliminary reference Earth model. Physics of the Earth and Planetary Interiors, 25, 297–356.

Fåk, B., and Dorner, B. (1997) Phonon line shapes and excitation energies. Physica B, 234, 1107-1108.

Fiquet, G., Badro, J., Guyot, F., Requardt, H., and Krisch, M. (2001) Sound velocities in iron to 110 gigapascals. Science, 291, 468-471.

Fukui, H., Katsura, T., Kuribayashi, T., Matsuzaki, T., Yoneda, A., Ito, E., Kudoh, Y., Tsutsui, S., and Baron, A.Q.R. (2008) Precise determination of elastic constants by high-resolution inelastic X-ray scattering. Journal of Synchrotron Radiation, 15, 618-623.

Hill, J.E., and Ruoff, A.L. (1965) Velocity of sound measurements in liquid metals. Review of Scientific Instruments, 36, 1465-1472.

Kamioka, H. (1983) Change of ultrasonic wave velocity in indium near the melting point. Journal of the Physical Society of Japan, 52, 2784-2789.

Komabayashi, T. (2014) Thermodynamics of melting relations in the system Fe-FeO at high pressure: Implications for oxygen in the Earth's core. Journal of Geophysical Research, 119, DOI: 10.1002/2014JB010980.

Mao, H.K., and Bell, P.M. (1986) Calibration of the ruby pressure gauge to 800 kbar under quasi-hydrostatic conditions. Journal of Geophysical Research, 91, 4673-4676.

Noguchi, M., Komabayashi, T., Hirose, K., and Ohishi, Y. (2013) High-temperature compression of $CaSiO_3$ perovskite to lowermost mantle conditions and its thermal equation of state. Physics and Chemistry of Minerals, 40, doi:10.1007/s00269-00012-00549-00261.

Reichert, H., Bencivenga, F., Wehinger, B., Krisch, M., Sette, F., and Dosch, H. (2007) High-frequency subsurface and bulk dynamics of liquid indium. Physical Review Letters, 98, 096104.

Sakaiya, T., Takahashi, H., Kondo, T., Kadono, T., Hironaka, Y., Irifune, T., and Shigemori, K. (2014) Sound velocity and density measurements of liquid iron up to 800 GPa: a universal relation between Birch's law coefficients for solid and liquid metals. Earth and Planetary Science Letters, 392, 80-85.

Scopigno, T., Balucani, U., Ruocco, G., and Sette, F. (2000) Density fluctuations in molten lithium: inelastic x-ray scattering study. Journal of Physics: Condensed Matter, 12, 8009-8034.

Scopigno, T., Ruocco, G., and Sette, F. (2005) Microscopic dynamics in liquid metals: The experimental point of view. Reviews of Modern Physics, 77, 881-933.

Shen, G.Y., Sata, N., Taberlet, N., Newville, M., Rivers, M.L., and Sutton, S.R. (2002a) Melting studies of indium: determination of the structure and density of melts at high pressures and high temperatures. Journal of Physics: Condensed Matter, 14, 10533-10540.

Shen, G.Y., Sata, N., Newville, M., Rivers, M.L., and Sutton, S.R. (2002b) Molar volumes of molten indium at high pressures measured in a diamond anvil cell. Applied Physics Letters, 81, 1411-1413.

Shibazaki, Y., Ohtani, E., Fukui, H., Sakai, T., Kamada, S., Ishikawa, D., Tsutsui, S., Baron, A.Q.R., Nishitani, N., Hirao, N., and Takemura, K. (2012) Sound velocity measurements in dhcp-FeH up to 70 GPa with inelastic X-ray scattering: Implications for the composition of the Earth's core. Earth and Planetary Science Letters, 313, 79-85.

Takemura, K. (1991) Effect of pressure on the lattice distortion of indium to 56 GPa. Physical Review B, 44, 545-549.

Umemoto, K., Hirose, K., Imada, S., Nakajima, Y., Komabayashi, T., Tsutsui, S., and Baron, A.Q.R. (2014) Liquid iron-sulfur alloys at outer core conditions by first-principles calculations. Geophysical Research Letters, 41, doi:10.1002/2014GL061233.

Vočadlo, L., Alfe, D., Gillan, M. J., and Price, D. G. (2003) The properties of iron under core conditions from first principles calculations. Physics of the Earth and Planetary Interiors, 140, 101-125.

494 **Figure captions**

495

496 **Figure 1.** Experimental *P-T* conditions. The pressures were determined by the ruby
497 fluorescence at 300 K and estimated from melting point at high temperature. The
498 squares show the *P-T* conditions of the IXS measurements. The dashed line represents
499 the *P-T* trajectory in each run. Note that in the first run, we operated two heating cycles
500 and the error bars apply to the second cycle. In the sixth run, the nominal pressures for
501 the IXS measurements should be taken as the maximum because the pressures might
502 have been lower than the *P-T* path. The melting curve of indium is from Shen et al.
503 (2002a) (the error bar is applied above 6.5 GPa).

504

505 **Figure 2.** A series of XRD images collected in the 2nd run. At 300 K, three diffraction
506 rings (101, 002, and 110) from solid indium were observed. At 603 K, the solid rings
507 became spotty due to grain growth. At 617 K, the major diffraction spots from solid
508 indium disappeared and instead a clear diffuse signal appeared indicating presence of
509 liquid. At 652 K, only the liquid diffuse signal was observed. Note that the thin
510 diffraction rings were from instruments on the X-ray path, not from the sample. The
511 contrast in each image was adjusted so that all the images would show similar

512 background-signal intensity ratios.

513

514 **Figure 3.** IXS spectra of liquid indium at 6.5 GPa and 710 K in the fifth run. The
515 momentum transfer ($Q$) values are indicated (in $nm^{-1}$). The peak at 22 meV and $Q$ =
516 $3nm^{-1}$ is the transverse acoustic (TA) mode from the diamond anvils.

517

518 **Figure 4.** $Q$-$E$ plots of liquid indium at different pressures at 710 K (This study) and at
519 1 bar and 443 K (Reichert et al., 2007).

520

521 **Figure 5**. Dispersion relation of liquid indium at 2.6 GPa and 710 K. The IXS data was
522 analyzed by the DHO model and current-current correlation function, $J(Q, E)$, model,
523 which are consistent each other. The two solid lines are fitted results with a linear and
524 sine functions.

525

526 **Figure 6.** LA velocity of indium from the IXS together with the existing data (Alatas et
527 al., 2008). The colored numbers are experimental temperatures. The open symbols are
528 the IXS data in the sixth run in which the pressure should be considered to be the
529 maximum estimate. Isothermal lines at 500, 700, and 900 K calculated from the EoS

530 are also plotted.

531

532 **Figure 7.** Compression curves of liquid indium calculated from the EoS. Experimental
533 data are also plotted: symbol, liquid at 710 K (Shen et al., 2002b); dashed line, solid at
534 300 K (Takemura, 1991). Since Shen et al. (2002b)'s liquid data show smaller volumes
535 than the solid phase at high pressures, we do not use their data for the fitting of liquid
536 EoS.

537

538 **Figure 8.** Velocity-density relations of liquid indium. Data sources are Hill and Ruoff
539 (1965), Alatas et al. (2008), Kamioka (1983), and this study. The experimental
540 temperatures are plotted (color). The open squares are the IXS data in the sixth run in
541 which the density should be considered to be the maximum estimate. Isothermal
542 velocities from the EoS in this study are also calculated at 500, 700, and 900 K.

543

544 **Figure 9.** Comparison in LA velocity for liquid indium between the IXS measurements
545 and calculations with the EoS ($c_0$). The numbers are experimental temperatures. The
546 uncertainty attached to the symbols incudes those in the EoS and in the experiments.
547 The open symbols are the IXS data in the sixth run in which the pressure should be the

548 maximum estimate; if the experimental pressures were lower, the density will be
549 smaller and hence, the velocity difference between the IXS and EoS will be smaller.
550
551 **Figure 10.** Velocity-density relations of liquid iron. The calculated LA velocities ($c_0$)
552 at 136-350 GPa and 5000, 6000, and 7000 K (Komabayashi, 2014) are plotted together
553 with shock wave experimental data (Brown and McQueen, 1986; Sakaiya et al., 2014).
554 The numbers are the temperatures. The LA velocity from the EoS is consistent with the
555 shock wave data points to 7228 K (Brown and McQueen, 1986). The isothermal lines
556 clearly show the temperature dependent velocity-density relations. The outer core data
557 (PREM) is also plotted (Dziewonski and Anderson, 1981).
558
559 **Figure 11.** Pressure-velocity relations for liquid iron. The data source is Komabayashi
560 (2014). The relations show no temperature dependence from 5000 to 7000 K, which
561 violates Birch's law.
562
563
564
565

**Table 1. Experimental conditions and sound velocity and density of indium.**

| | Pressure GPa | Temperature K | Vp (IXS with sine fit) m/s | Vp (IXS with linear fit) m/s | Vp (EoS)[a] m/s | Density g/cm$^3$ | Phase |
|---|---|---|---|---|---|---|---|
| *1st run* | 1.0 | 300 | 2492 ± 38 | - | - | 7.46[b] | solid |
| | 1.8 | 517 | 2546 ± 43 | 2544 ± 46 | 2490 | 7.32 | liquid |
| *quench and reheat* | | | | | | | |
| | 2.2 ± 0.2[c] | 612 | 2585 ± 42 | 2573 ± 44 | 2512 | 7.33 | liquid |
| | 2.6 ± 0.5[c] | 710 | 2637 ± 42 | 2594 ± 44 | 2529 | 7.33 | liquid |
| | | | | | | | |
| *2nd run* | 3.0 | 300 | 2706 ± 38 | - | - | 7.76[b] | solid |
| | 4.9 | 710 | 2800 ± 42 | 2766 ± 44 | 2743 | 7.70 | liquid |
| | 4.6 | 650 | 2833 ± 42 | 2765 ± 44 | 2732 | 7.70 | liquid |
| | | | | | | | |
| *3rd run* | 5.0 | 300 | 2946 ± 48 | - | - | 8.02[b] | solid |
| | | | | | | | |
| *4th run* | 6.7 | 710 | 3116 ± 67 | 3023 ± 34 | 2884 | 7.96 | liquid |
| | | | | | | | |
| *5th run* | 6.5 | 710 | 3078 ± 46 | 3040 ± 46 | 2873 | 7.94 | liquid |
| | | | | | | | |
| *6th run* | 2.1[d] | 573 | 2451 ± 58 | 2403 ± 41 | 2488 | 7.34 | liquid |
| | 1.6[d] | 673 | 2438 ± 58 | 2385 ± 41 | 2411 | 7.18 | liquid |
| | 1.2[d] | 773 | 2280 ± 57 | 2251 ± 41 | 2331 | 7.03 | liquid |
| | 0.5[d] | 923 | 2259 ± 57 | 2216 ± 41 | 2212 | 6.76 | liquid |

[a] The sound velocity was obtained from the equation of state for the liquid phase.

[b] The solid density was derived from the equation of state by Takemura (1991).

[c] Uncertainty is large because the pressure at 300 K is unknown.

[d] Nominal pressure and density are maximum estimates.

566

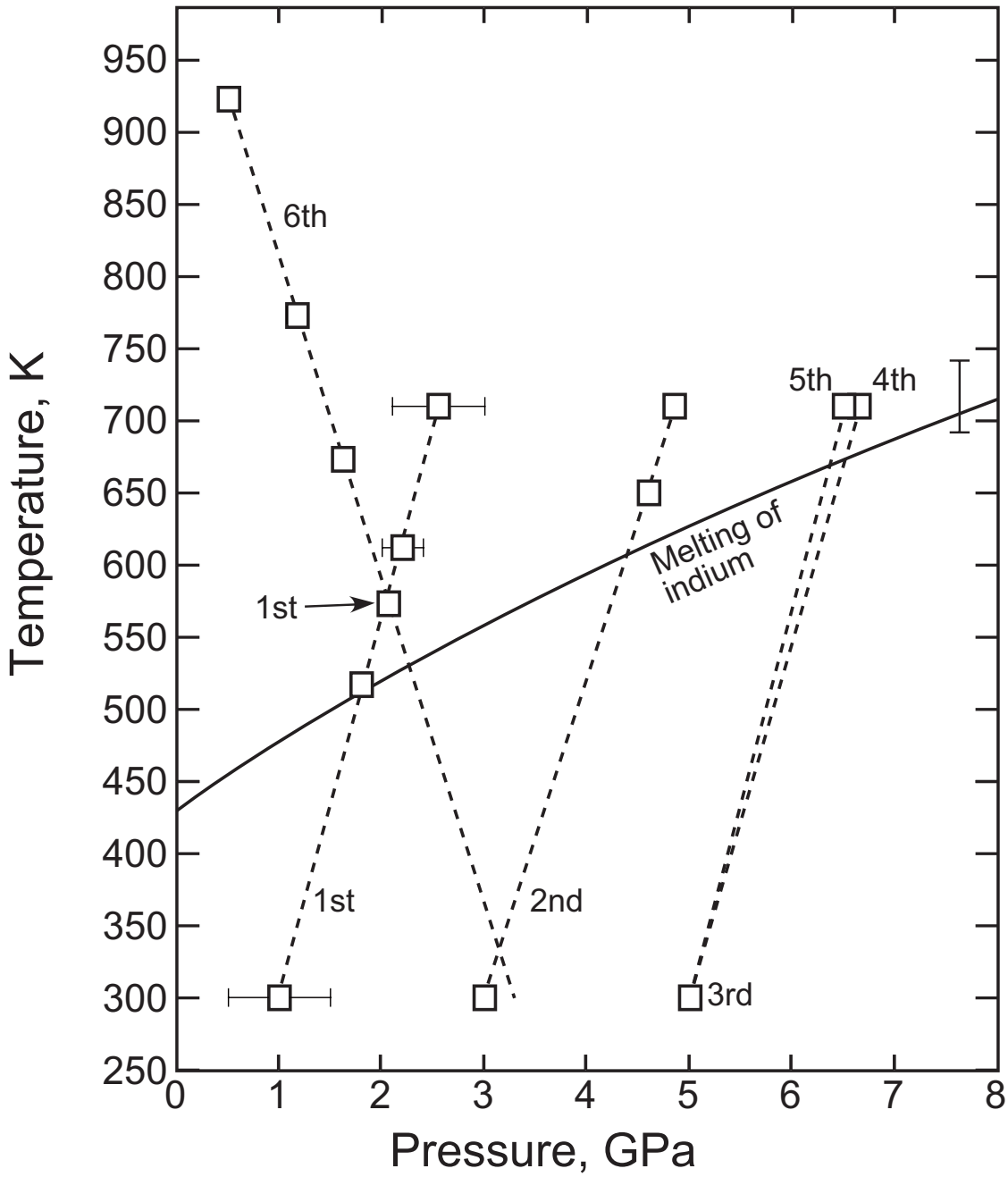
Temperature, K
Pressure, GPa
950
900
850
800
750
700
650
600
550
500
450
400
350
300
250
0
1
2
3
4
5
6
7
8
6th
5th
4th
1st
Melting of indium
1st
2nd
3rd

figure 1

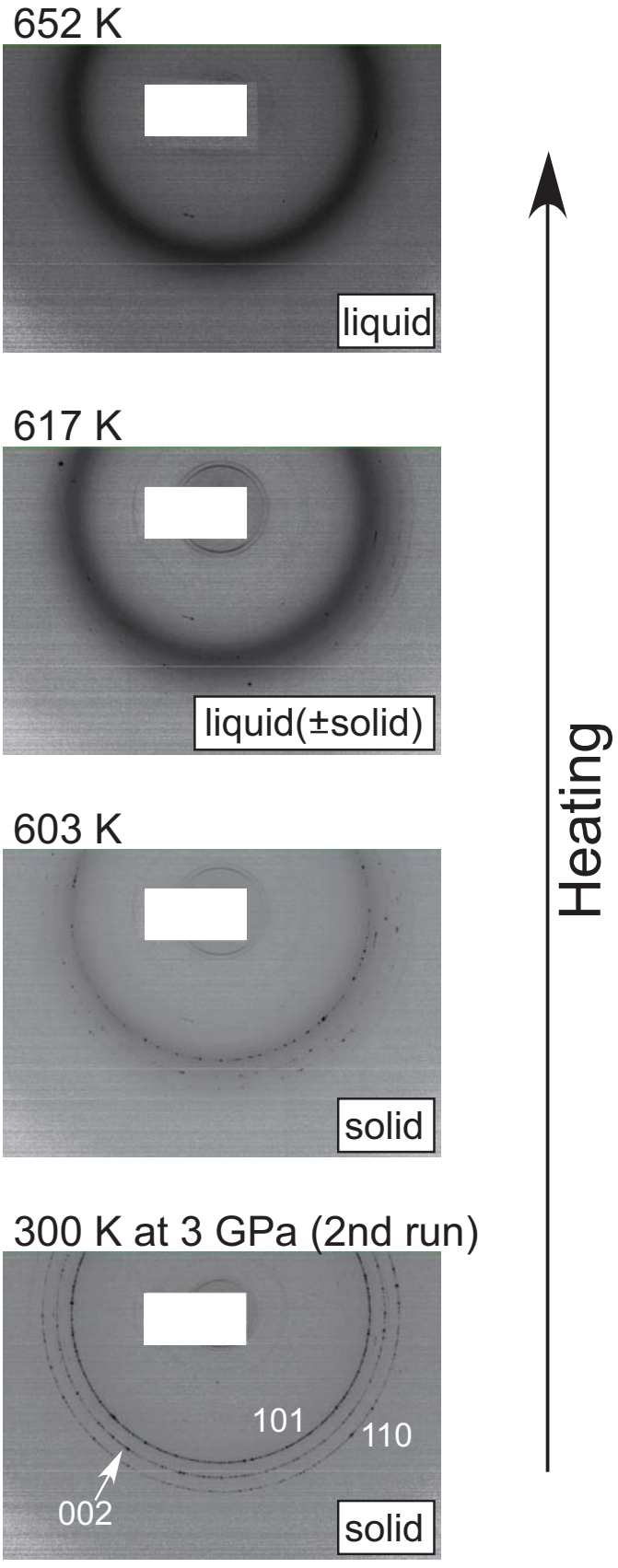
652 K
liquid
617 K
liquid(±solid)
603 K
solid
300 K at 3 GPa (2nd run)
101
110
002
solid
Heating

fig. 2

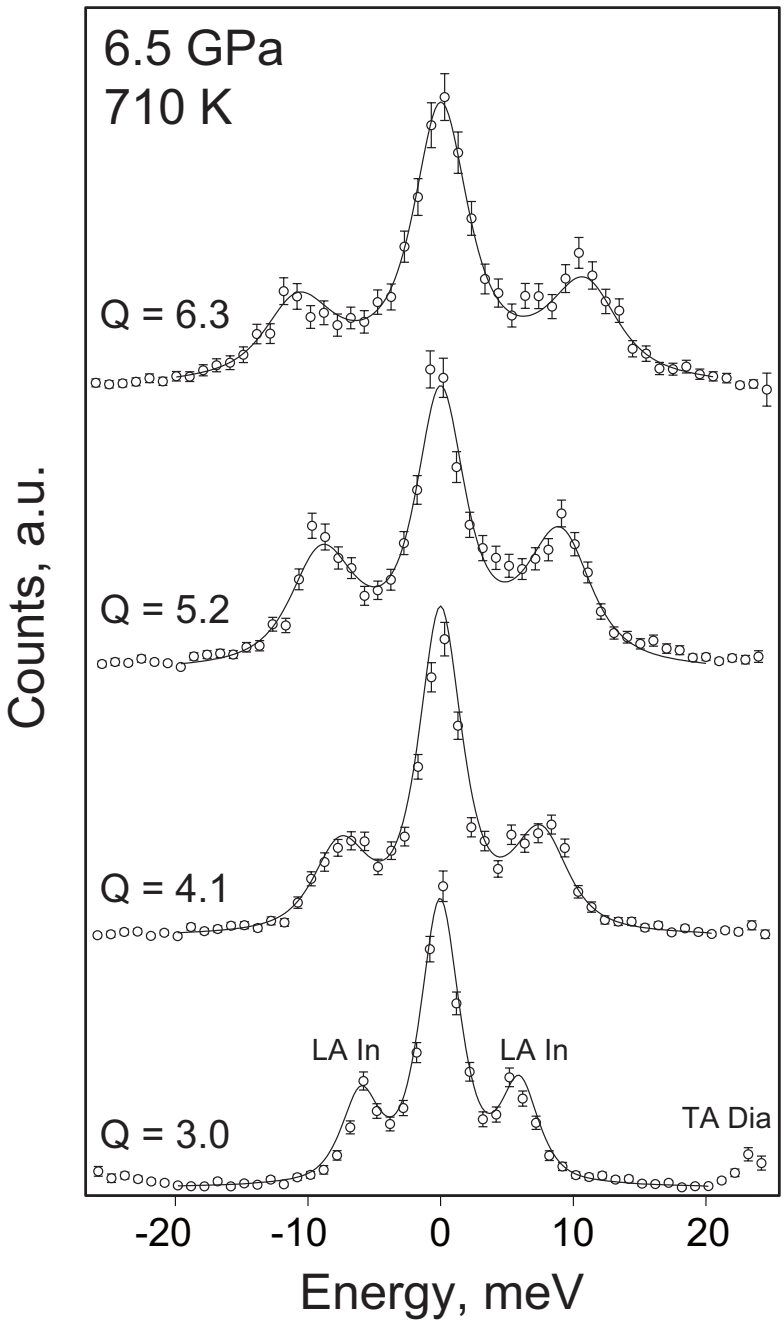
6.5 GPa
710 K
Q = 6.3
Q = 5.2
Q = 4.1
Q = 3.0
LA In
LA In
TA Dia
Counts, a.u.
-20
-10
0
10
20
Energy, meV

fig. 3

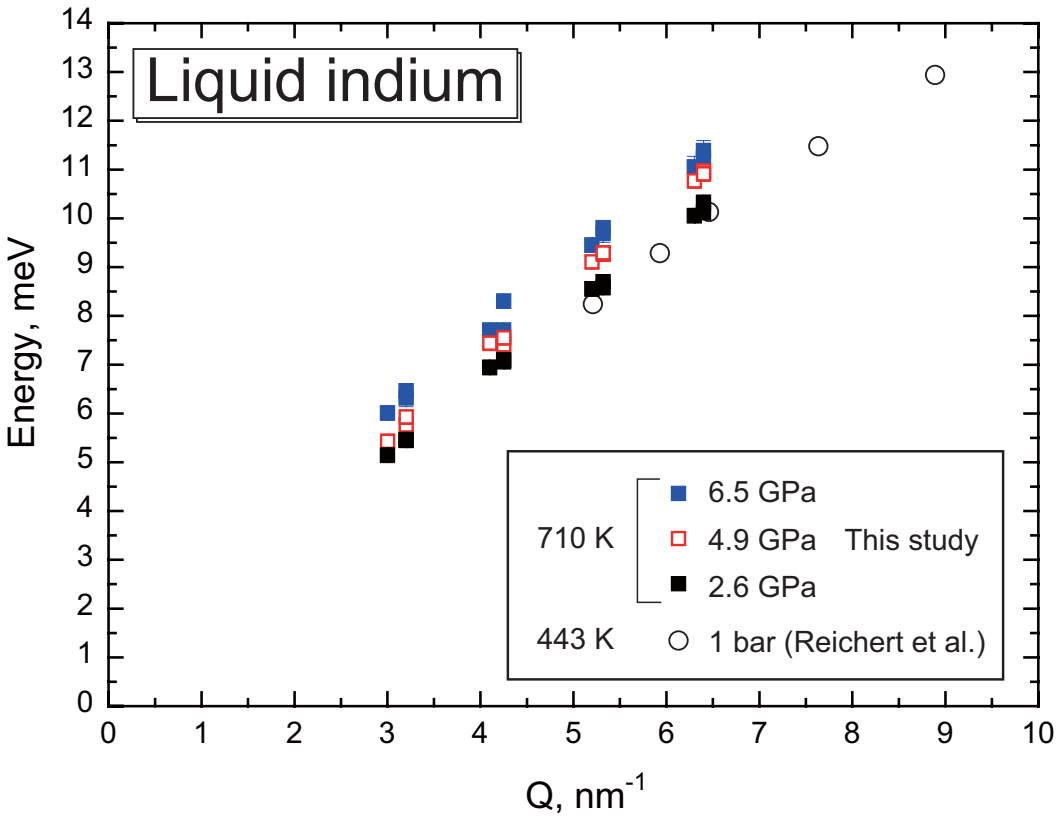
Liquid indium
Energy, meV
Q, nm-1
710 K
6.5 GPa
4.9 GPa
2.6 GPa
This study
443 K
1 bar (Reichert et al.)

figure 4

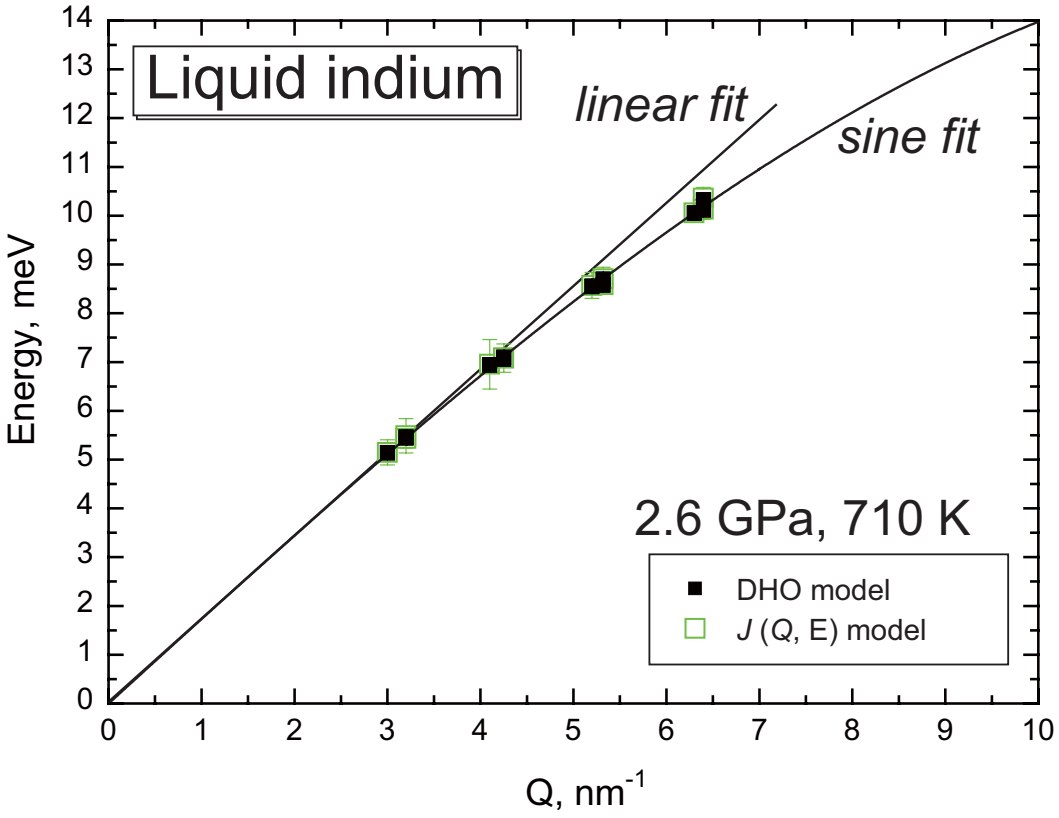
Liquid indium
linear fit
sine fit
2.6 GPa, 710 K
DHO model
J (Q, E) model
Energy, meV
Q, nm-1
0
1
2
3
4
5
6
7
8
9
10
11
12
13
14

figure 5

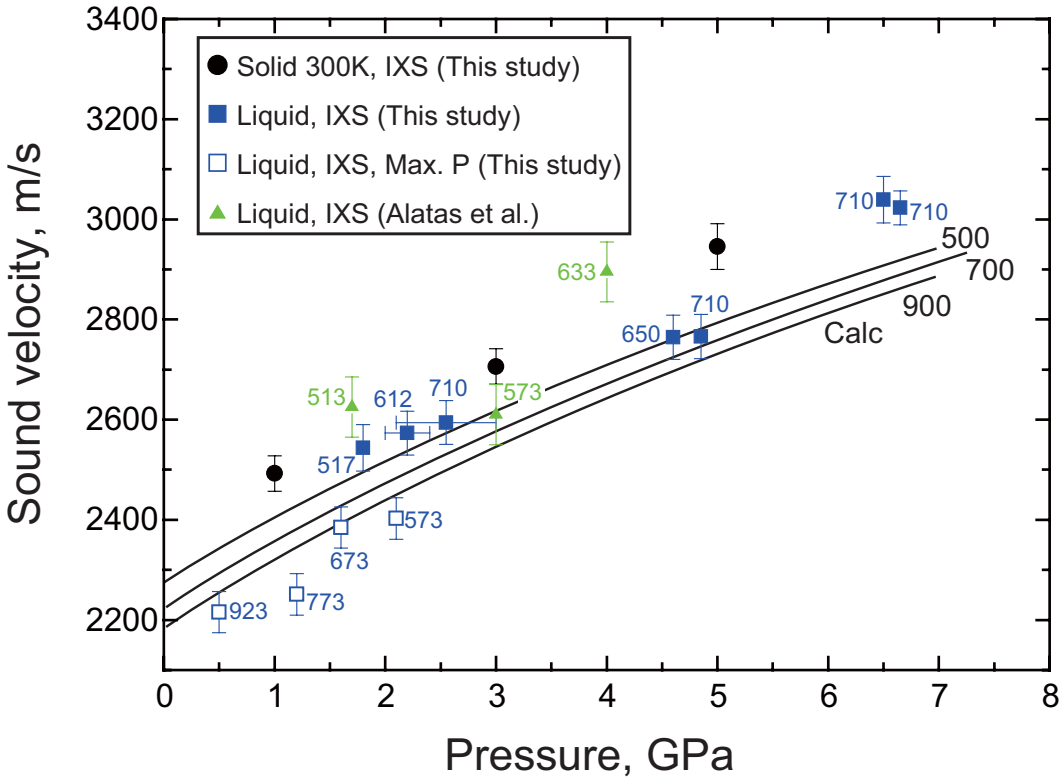
Solid 300K, IXS (This study)
Liquid, IXS (This study)
Liquid, IXS, Max. P (This study)
Liquid, IXS (Alatas et al.)
Sound velocity, m/s
Pressure, GPa
3400
3200
3000
2800
2600
2400
2200
0
1
2
3
4
5
6
7
8
500
700
900
Calc
710
710
633
710
650
513
612
710
573
517
573
673
773
923

figure 6

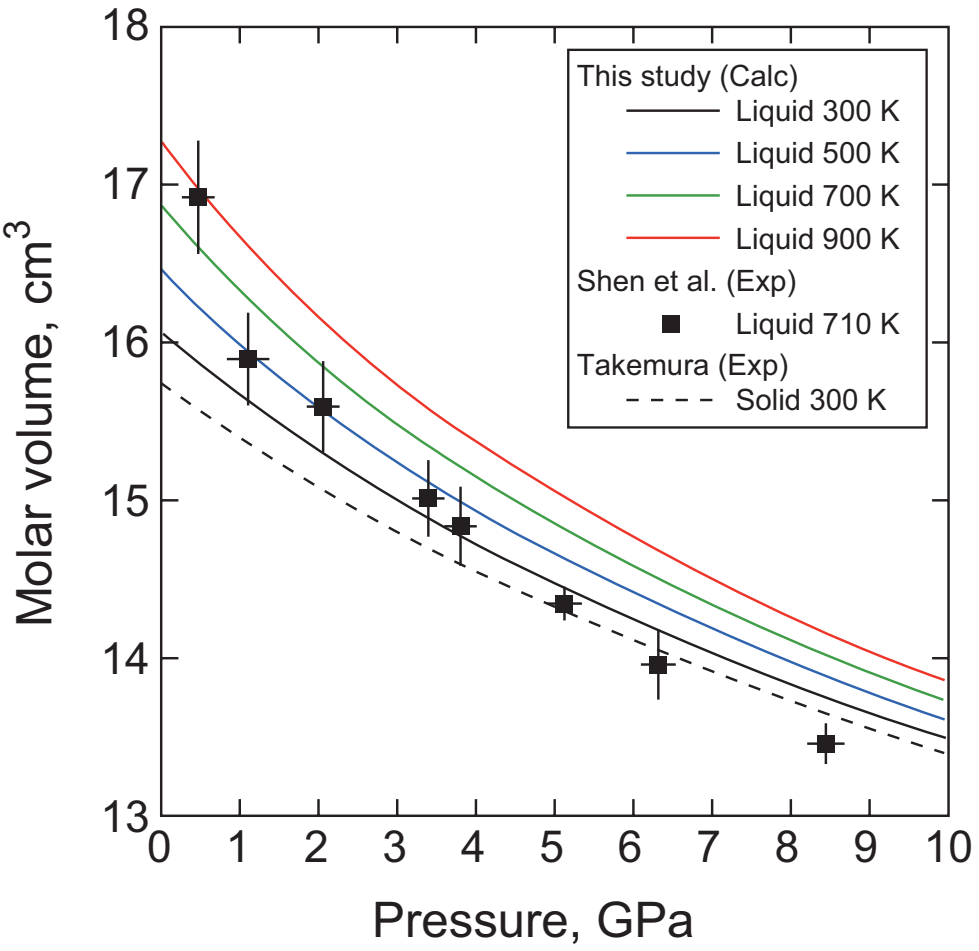
Molar volume, cm3
Pressure, GPa
18
17
16
15
14
13
0
1
2
3
4
5
6
7
8
9
10
This study (Calc)
Liquid 300 K
Liquid 500 K
Liquid 700 K
Liquid 900 K
Shen et al. (Exp)
Liquid 710 K
Takemura (Exp)
Solid 300 K

figure 7

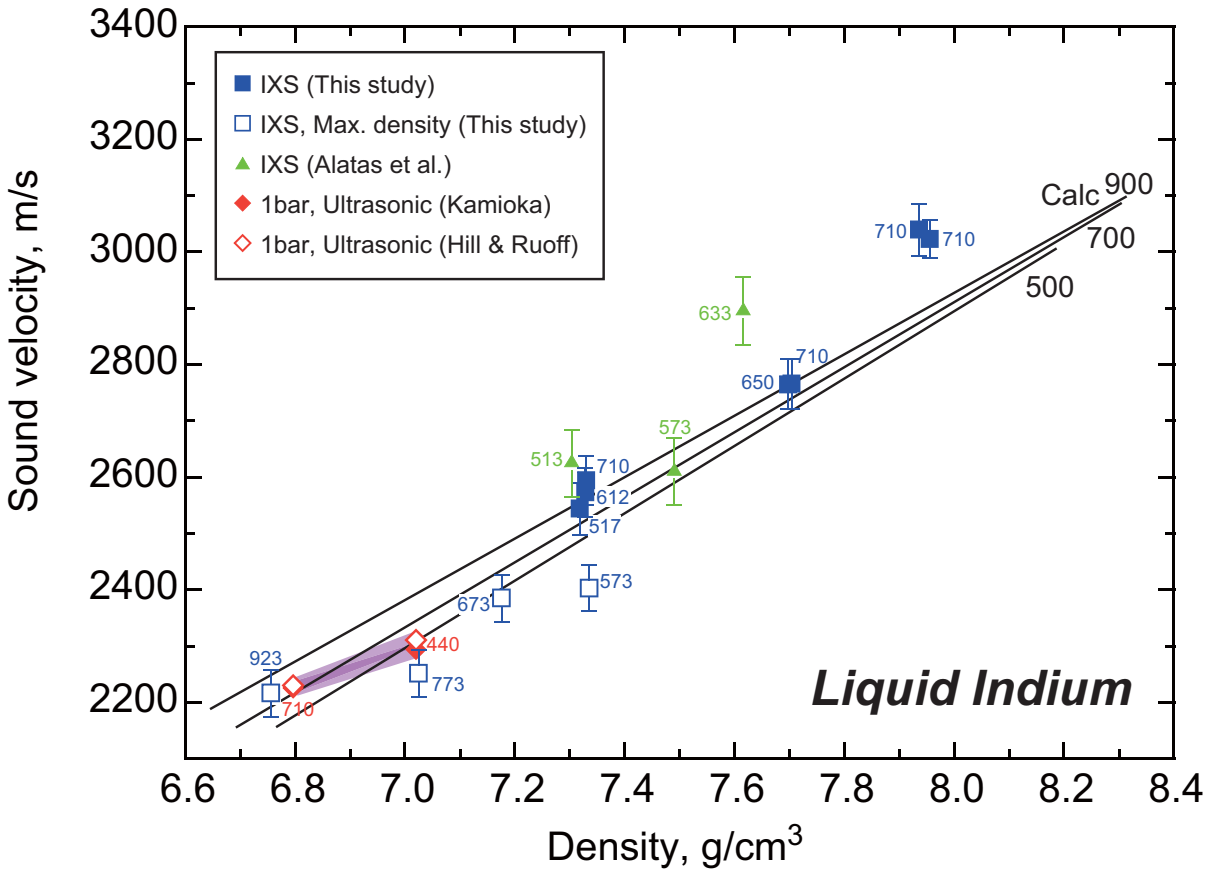
IXS (This study)
IXS, Max. density (This study)
IXS (Alatas et al.)
1bar, Ultrasonic (Kamioka)
1bar, Ultrasonic (Hill & Ruoff)
Calc
900
700
500
Liquid Indium
Sound velocity, m/s
Density, g/cm3
3400
3200
3000
2800
2600
2400
2200
6.6
6.8
7.0
7.2
7.4
7.6
7.8
8.0
8.2
8.4
710
710
633
710
650
573
513
710
612
517
573
673
923
440
773
710

figure 8

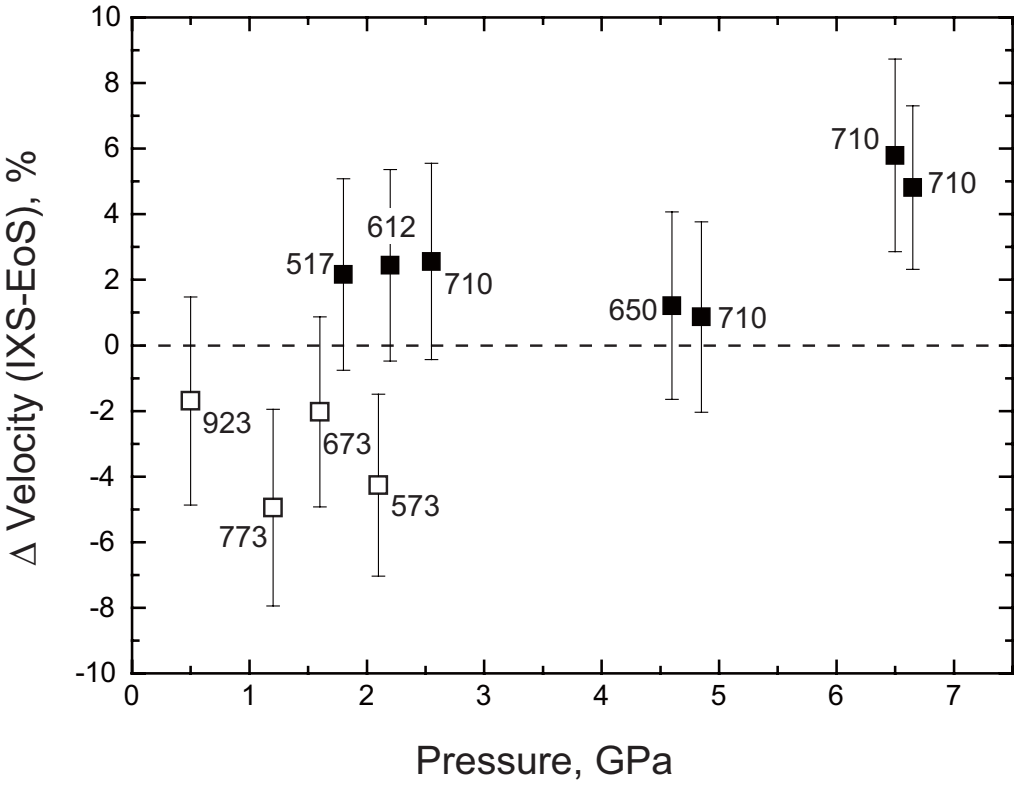
Δ Velocity (IXS-EoS), %
Pressure, GPa
923
773
673
573
517
612
710
650
710
710
710

figure 9

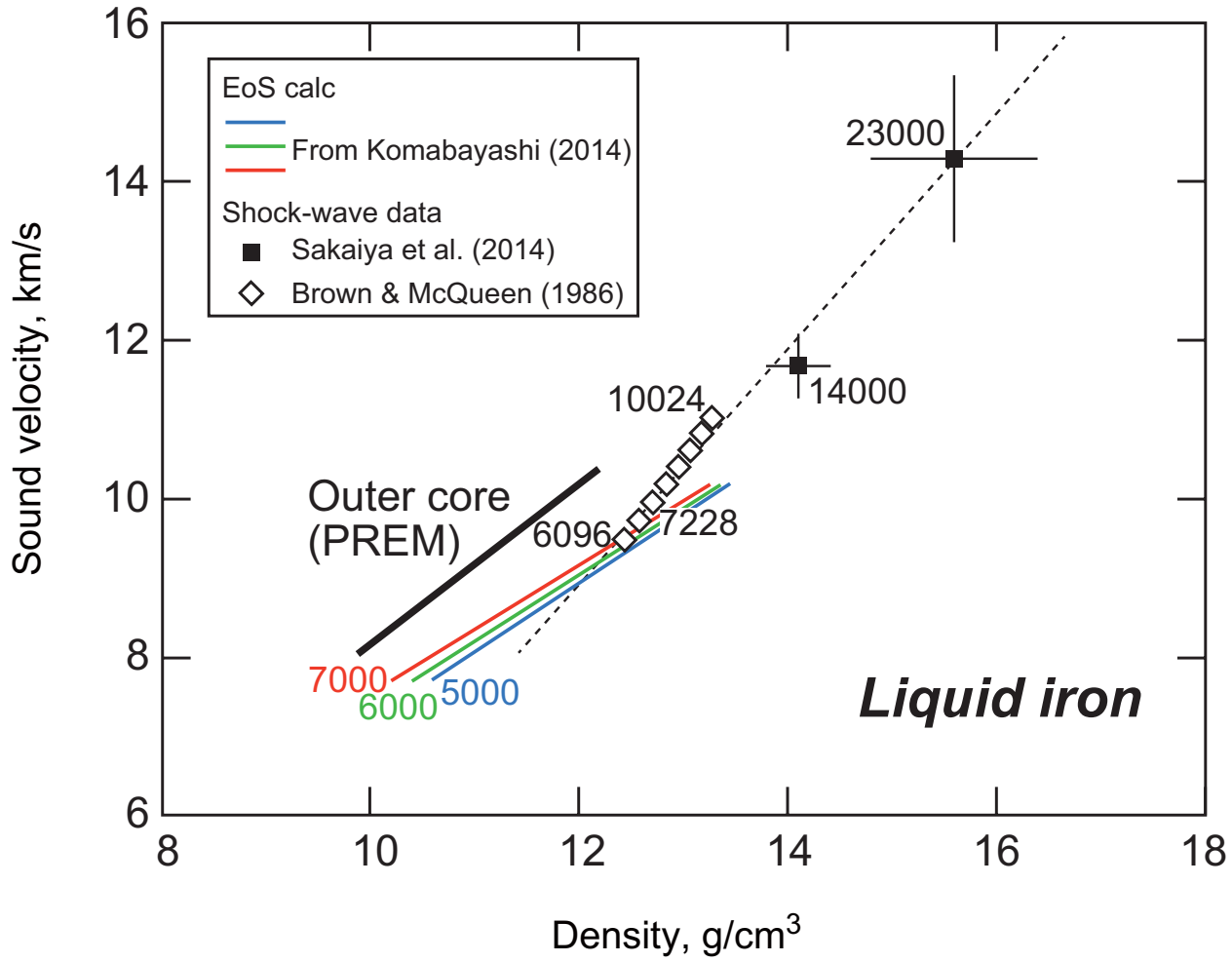
EoS calc
From Komabayashi (2014)
Shock-wave data
Sakaiya et al. (2014)
Brown & McQueen (1986)
23000
14000
10024
6096
7228
Outer core
(PREM)
7000
6000
5000
Liquid iron
Sound velocity, km/s
Density, g/cm3
16
14
12
10
8
6
8
10
12
14
16
18

figure 10

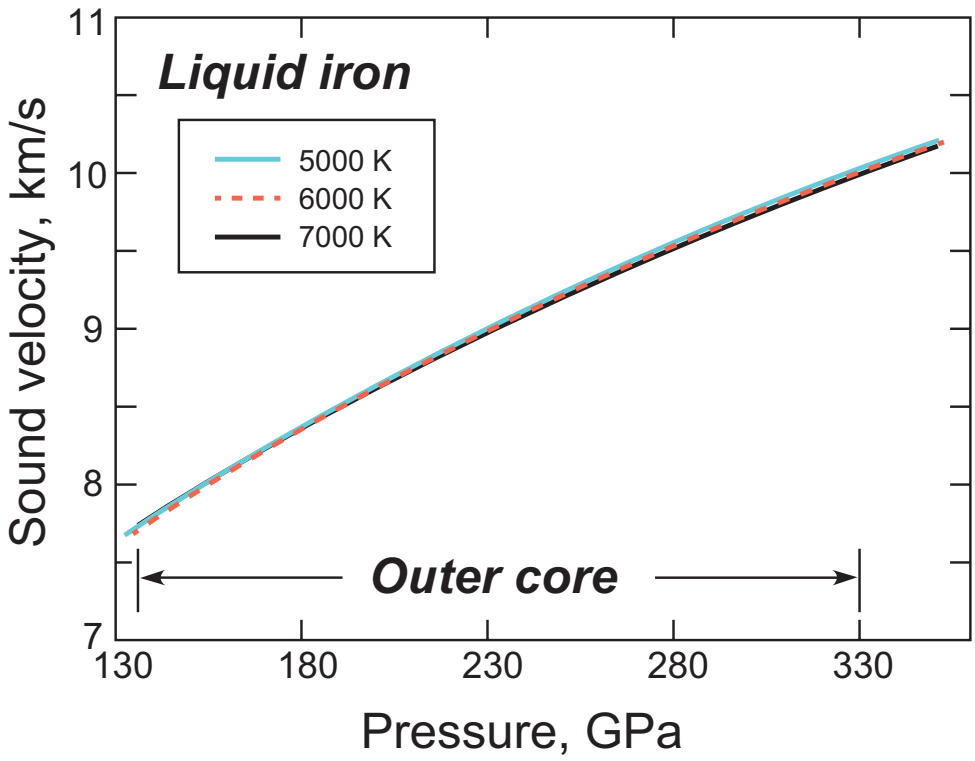
Liquid iron
5000 K
6000 K
7000 K
Outer core
Sound velocity, km/s
Pressure, GPa
11
10
9
8
7
130
180
230
280
330

figure 11